ISPRS Journal of Photogrammetry and Remote Sensing 168 (2020) 221–235

Contents lists available at ScienceDirect

ISPRS Journal of Photogrammetry and Remote Sensing

journal homepage: www.elsevier.com/locate/isprsjprs

Response of winter wheat to spring frost from a remote sensing perspective: Damage estimation and influential factors

Shuai Wang [a], Jin Chen [a,*], Yuhan Rao [b], Licong Liu [a], Wenqing Wang [a], Qi Dong [a]

[a] State Key Laboratory of Earth Surface Processes and Resource Ecology, Institute of Remote Sensing Science and Engineering, Faculty of Geographical Science, Beijing Normal University, Beijing 100875, China
[b] North Carolina State University, North Carolina Institute for Climate Studies, Asheville, NC 28801, United States

ARTICLE INFO

Keywords:
Spring frost
Winter wheat
Damage assessment
Remote sensing
North China

ABSTRACT

Spring frost is one of the major weather-related threats to winter wheat. The damage to winter wheat caused by spring frost is aggravated by the increase in extreme weather events and the advance of spring phenology driven by a warming climate. Until recently, studies of frost damage were primarily based on controlled field experiments and crop model simulations, which cannot accurately represent the real frost damage suffered by winter wheat in the natural environment. In this study, a remote sensing-based spring frost damage index (SFDI) was proposed to rapidly and effectively quantify the impact of spring frost on winter wheat at the provincial scale. Compared with the existing methods, the SFDI is easy to implement with widely available remotely sensed vegetation index (VI) time-series data. It can be used to assess spring frost damage to winter wheat in near real-time to allow a rapid response. Although the SFDI was developed for winter wheat and spring frost, it has the potential to be extended to other agricultural hazards and crop types through careful adjustments to the design. We assessed the performance of SFDI using a spring frost event that occurred from April 3–7, 2018, in North China as a case study. The results showed that the severely damaged areas were mainly located at the junction of Hebei, Henan, and Shandong provinces, especially in western Shandong Province. The result showed good agreement with the proxy data retrieved from the national archives of regional newspaper reports about the event. The validity of the new index (SFDI) was also verified against the reduction in county-level crop production. Additionally, we used multivariate linear regression (MLR) and geographically weighted regression (GWR) to identify the key factors affecting the spatial variation in SFDI. The results indicated that the growth status of winter wheat before spring frost and the amount of precipitation during the frost event were the two major factors affecting the severity of frost damage to winter wheat, followed by the accumulated frost degree-days and soil moisture. This suggests that proper management of the crop growth rate after winter wheat greening and adequate soil moisture (from irrigation and precipitation) before and during the spring frost period could greatly alleviate the damage of spring frost to winter wheat.

1. Introduction

North China, which has a large cultivated area of winter wheat, accounts for two-thirds of the wheat production in the country, playing a dominant role in ensuring China's food security (Jin, 1996). In recent years, winter wheat in this region has experienced increasingly extreme weather events during its life cycle. Among these extreme weather events, spring frost, which is characterized as a short duration of freezing temperatures during the jointing and heading stages of winter wheat, leads to great declines in both crop yield and quality (Frederiks et al., 2015; Crimp et al., 2016; Xiao et al., 2018). The adverse effects of spring frost on the crop include not only damage to the chlorophyll content and photosynthetic capacity of the leaves (Li et al., 2015) but also the reduction of the tiller survival rate, number of spikes, and kernel number per spike (XIANGNAN Li et al., 2015; X. Li et al., 2015; Zheng et al., 2015). Model analysis suggested that grain yields may decline by 7% over the entire winter wheat growing region of China for each 1 °C·day increase in accumulated frost degree-days (Xiao et al., 2018). When considering climate change, global warming would seem to reduce the occurrence of frost events. However, this does not necessarily reduce the loss of winter wheat caused by spring frost (Gu et al., 2008; Eccel et al., 2009; Zheng et al., 2015) because global warming

* Corresponding author.
E-mail address: chenjin@bnu.edu.cn (J. Chen).

https://doi.org/10.1016/j.isprsjprs.2020.08.014
Received 7 May 2020; Received in revised form 13 August 2020; Accepted 14 August 2020
Available online 27 August 2020

accelerates vegetative development and causes the frost-sensitive stages to develop earlier due to a warmed winter and spring (Li et al., 2015; Xiao et al., 2018). Consequently, the advancement of winter wheat growth and the increasing occurrence of extreme weather events along with global warming, especially in winter and spring, simultaneously lead to a greater risk of spring frost to winter wheat (Trnka et al., 2014; Zheng et al., 2018). Accordingly, effectively monitoring and assessment of the impact of spring frost on winter wheat at a large scale is of great significance for mitigating crop losses for food security and the economy.

Previous studies have largely been concerned with the spatiotemporal patterns of spring frost and their impacts on wheat yield in China (Li et al., 2015; Xiao et al., 2018). Xiao et al. (2018) analyzed long-term historical climate data and yield records and provided a comprehensive assessment of frost risk from a meteorological perspective. However, the risk-based study did not directly analyze the immediate response of winter wheat during spring frost events. Therefore, this study could not be applied to quantify the direct spring frost damage to winter wheat in near real time. Current studies on spring frost damage to winter wheat have primarily depended on controlled field experiments (Sutka, 1994; Fedoulov, 1997; Whaley et al., 2004; Wang et al., 2012; XIANGNAN Li et al., 2015a, 2015b; X. Li et al., 2015) and crop model simulations (Lazăr et al., 2005; Zhang et al., 2012; Zheng et al., 2015). Through controlled field experiments, the impacts of spring frost on winter wheat growth can be directly observed and measured following the strategy of changing one factor in an experiment while keeping the others fixed. For example, Meng et al. (2017) found that freezing injury had the highest impact on winter wheat yield under a soil surface drying treatment through a joint experiment that involved controlling both soil surface moisture and frost intensity in cryogenic chambers. Zheng et al. (2018) conducted two years of controlled freezing experiments with different freezing temperatures and durations. Their results revealed that the effects of freezing duration on the mortality of plants and tillers and the effects on the grain yield per pot were much more severe under lower temperatures. Nuttall et al. (2019) used mobile frost chambers to examine the impact of simulated frost at the reproductive stage on wheat growth and yield. The results showed that grain number and yield were reduced by 8.8% and 7.2%, respectively, for each degree Celsius below zero when frost treatments were applied at the anthesis stage. A more recent study evaluated the response of the wheat canopy hyperspectral reflectance to low temperature injury and estimated the yield losses (Xie et al., 2020). Although this study provided very valuable insight, it only used hyperspectral data collected from a controlled field-based experiment, which might be difficult to implement and reproduce at a large scale with existing remotely sensed data due to the limitations of instruments and complex atmospheric conditions. Controlled field experiments are indispensable for understanding the physiological and ecological mechanisms of spring frost damage. However, this approach can neglect the compounding impacts of other factors and cannot reflect the real growth conditions in the natural environment.

Process-based crop model simulations are another way to evaluate spring frost damage to winter wheat by changing temperature conditions to represent spring frost and then simulating the growth and yield of winter wheat. Zheng et al. (2015) used the APSIM-Wheat crop model to simulate the frost impact on wheat yield. Their results suggested that the yield decreased by up to 1–2% per year in certain regions of Australia due to frost damage, and the frost impacts on wheat yield were related not only to temperature but also to the phenology of winter wheat. Bergjord Olsen et al. (2018) employed the FROSTOL model to explore how soil temperature, snow depth, and the grown cultivar's maximum attainable level of frost tolerance affected the frost damage to winter wheat. The advantages of crop model simulations are that the spring frost intensity can be controlled to desired levels and that the interactions between spring frost and other factors can be well addressed. However, as Barlow et al. (2015) noted, the existing crop models are still not sophisticated enough to adequately account for the impact of extreme climate events on crop growth. The calibration of many model parameters is also problematic, and sometimes models are only applicable to specific small regions, which can introduce great uncertainty in simulation results. Therefore, direct observation and quantification of spring frost damage to winter wheat in the natural environment are urgently needed and can be further used to estimate yield loss and improve field management in subsequent growth processes.

In recent years, remote sensing has become one of the most powerful tools for monitoring the impacts of natural hazards on agriculture (Duveiller and Defourny, 2010; Rojas et al., 2011; Huang et al., 2014; Zhang et al., 2017) since it offers relevant information over large areas in a rapid and cost-effective manner. More importantly, this type of monitoring can include the combined impacts of various factors in the natural environment. The advantages of remote sensing techniques have prompted a series of related studies using remotely sensed data to monitor the impacts of spring frost on vegetation. Gu et al. (2008) found that the impacts of the 2007 spring freeze on vegetation development in the United States could be identified by reduced normalized difference vegetation index (NDVI) values after the event. Menzel et al. (2015) analyzed the time series of a greenness index extracted from webcam pictures of a forest stand and revealed the close link between spring frost damage and phenological variation. Following their ideas, several studies also used the vegetation index (VI) and land surface temperature (LST) to evaluate spring frost damage and further analyzed the influential factors using various methods, such as support vector machine (SVM), recurrent neural network (RNN) and NDVI differencing techniques (de Simões et al., 2015; Nolè et al., 2018; Bascietto et al., 2018; 2019; Allevato et al., 2019). Although these studies were not specific to winter wheat, they showed great potential for using the differences in the vegetation index before and after spring frost to monitor spring frost damage to winter wheat. Despite the potential, a general index to quantify spring frost damage has still not been developed due to the lack of a commonly accepted baseline to be compared after spring frost, especially for winter wheat. Moreover, how environmental factors (e.g., temperature and soil moisture) and vegetation growth conditions (e.g., phenology) jointly affect spring frost damage has yet to be completely explored using remotely sensed data at a large scale.

To address the abovementioned problems, the objectives of this study are two-fold: 1) to develop a remotely sensed VI-based damage indicator for quantifying spring frost damage to winter wheat at the provincial scale and 2) to identify key biotic and abiotic factors that affect regional variations in spring frost damage to the crop. Although this study aimed to find a flexible and efficient method to assess the damage of spring frost to winter wheat, it is not our intent to use this method to replace indispensable field surveys to understand the damage. The first objective provides a general method for effectively monitoring natural hazard impacts on agriculture, which ideally can be extended to other hazards and crop types (Section 2). The developed index was implemented for a spring frost event that occurred from April 3–7, 2018, in North China as a case study (Section 3, 4). The second objective will be helpful for recommending countermeasures to alleviate the impact of spring frost on winter wheat cultivation (Section 4, 5).

2. Methodology

2.1. Theoretical framework

The vegetation index (VI), which is calculated from the absorptive and reflective features of vegetation (e.g., the red and near-infrared (NIR) bands), is commonly used to monitor vegetation rigor and represent crop growth status (Tucker, 1979; Huete et al., 2002). A time series of remotely sensed VI (hereafter called the VI curve) can reflect the status of winter wheat throughout its growth cycle from sowing to harvest (Fig. 1).

During spring and early summer, winter wheat experiences the

jointing and heading stages, and its VI curve exhibits a continuous upward trend under normal environmental conditions (solid curve in Fig. 1). However, in the case of a spring frost event, which is characterized as a sudden decrease in temperature with a duration of several days, the spectral signature of winter wheat will be affected by significant changes due to decreasing leaf chlorophyll, leaf dehydration, and even wilting (Snyder and de Melo-Abreu, 2005; Meng et al., 2017). As a result, the VI curve will display a sudden drop, and such a drop can last for a certain period before recovering (dashed curve in Fig. 1). Theoretically, if we can obtain a VI curve without spring frost impact (hereafter referred to as the reference VI curve), the spring frost damage can be quantified by calculating the difference between the reference VI curve and the actual VI curve affected by spring frost. Based on this concept, the spring frost damage index (SFDI) was developed in this study to answer the main question: how much damage does winter wheat suffer from a spring frost event? The impact of a frost event on winter wheat starts with the initiation of the event, which can be observed from meteorological records or forecasts, and can persist beyond the duration of the spring frost event. To the best of our knowledge, there is not a well-established criterion for determining the end of the spring frost impact period. In this study, we used the date when the VI curve reached a maximum as the end of the impact period. Although the frost damage to the crop may be long-lasting for crop growth, the signal is difficult to distinguish after this date, when the winter wheat enters the grouting stage, which leads to a decline in the VI due to decreasing chlorophyll content (Fig. 1). Fig. 2 provides a conceptual schema for developing SFDI with detailed steps presented as follows.

2.1.1. VI calculation

There are many VIs that represent crop growth while limiting the noise from the soil background and atmosphere. Considering data availability, three VIs were selected for this study: NDVI (Tucker, 1979), the enhanced vegetation index (EVI) (Huete et al., 2002) and the normalized difference phenology index (NDPI) (Wang et al., 2017). The equations of the three VIs are listed below.

$$NDVI = \frac{\rho_{NIR} - \rho_{red}}{\rho_{NIR} + \rho_{red}} \tag{1}$$

$$EVI = 2.5 \cdot \frac{\rho_{NIR} - \rho_{red}}{\rho_{NIR} + C_1 \cdot \rho_{red} - C_2 \cdot \rho_{blue} + L} \tag{2}$$

$$NDPI = \frac{\rho_{NIR} - (0.74 \cdot \rho_{red} + 0.26 \cdot \rho_{SWIR})}{\rho_{NIR} + (0.74 \cdot \rho_{red} + 0.26 \cdot \rho_{SWIR})} \tag{3}$$

where ρ_{blue}, ρ_{red}, ρ_{NIR} and ρ_{SWIR} are the atmospherically corrected surface reflectances for blue, red, NIR, and shortwave-infrared (approximately 1.5 μm, SWIR) bands, respectively. C_1, C_2, and L are the coefficients and are set as L = 1, C_1 = 6, and C_2 = 7.5 according to the standard MODIS EVI product. These three VIs can be calculated from reflectance data or are directly provided as operational VI products, except NDPI, by commonly used remotely sensed data, including MODIS, Sentinel, SPOT-VGT, and Landsat TM/ETM+. In addition to the most widely used NDVI and EVI, the newly developed NDPI was included here because of its considerable advantages in minimizing the impacts of snow and soil background on VIs (Wang et al., 2017; Chen et al., 2019).

2.1.2. Reference VI curve

To quantitatively analyze the VI response to spring frost, it was necessary to obtain a reference VI curve, which can represent the typical growth cycle of winter wheat that has not been affected by spring frost. Since the reference VI curve cannot be obtained directly in the frost year, an assumption was carefully made that a multiyear average VI curve calculated from frost-free years could be used to approximate a reference VI curve. However, it should be noted that the multiyear average VI curve cannot perfectly represent the reference VI curve of a frost year because farmers' cultivation practices and climatic conditions vary yearly. Thus, the shape model fitting (SMF) method (Sakamoto et al., 2010, 2013) was used here to derive the reference VI curve by adjusting the multiyear average VI curve to account for these various factors.

First, we applied the Savitzky-Golay (SG) filter method (Chen et al., 2004) to the original VI curves to effectively reduce the noise in the VI curves, which was primarily caused by cloud contamination and poor atmospheric conditions (Pettorelli et al., 2005). Then, a multiyear average VI curve was calculated by simple averaging of the VI curves of frost-free years. To avoid the influence of outliers, only the VI values within the upper and lower quartiles of the frost-free curves were used here (Fig. 2a). It is evident that the multiyear average VI curve monotonically increases during spring and early summer, which is consistent with the ideal growth trajectory of winter wheat under normal conditions (solid line in Fig. 1). Thus, the multiyear average VI curve could be considered a candidate for the reference VI curve. The multiyear average VI curve was then defined as a shape model for the reference VI curve (Sakamoto et al.; 2010, 2013, Sakamoto, 2018).

As Fig. 2b shows, there were still notable differences between the shape model and the actual frost-year VI curve, in terms of both the magnitude (Y-axis) and the crop growth cycle (X-axis). These differences were likely caused by varying climatic conditions and changes in farmers' cultivation practices during the frost year. To adjust for these differences, the shape model was then geometrically scaled following Eq. (4) to match the SG-filtered frost-year VI as closely as possible (Fig. 2c).

$$h(x) = s_y \times \{ g(s_x \times (x + t_0)) \} \tag{4}$$

where the function $g(x)$ refers to the shape model (orange curve in

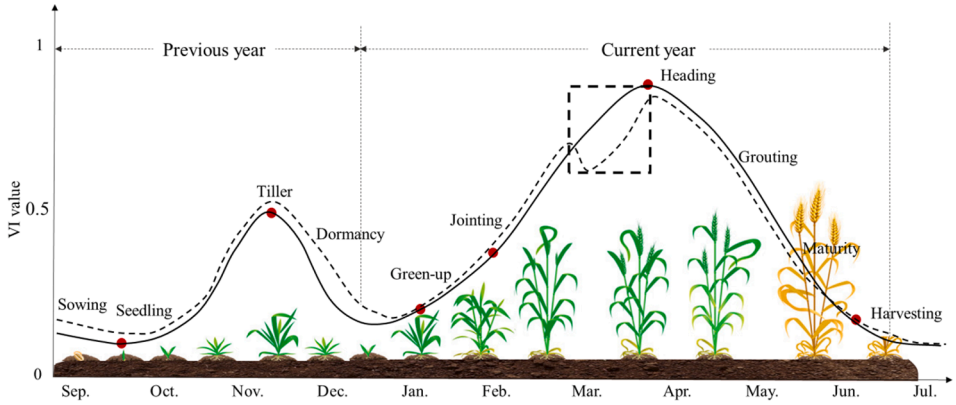

Fig. 1. A typical VI curve (solid line) of winter wheat and the VI curve (dashed line) in a year where spring frost occurred. The VI curve enclosed by the dashed box emphasizes that the VI curve affected by spring frost declines dramatically compared with the normal VI curve.

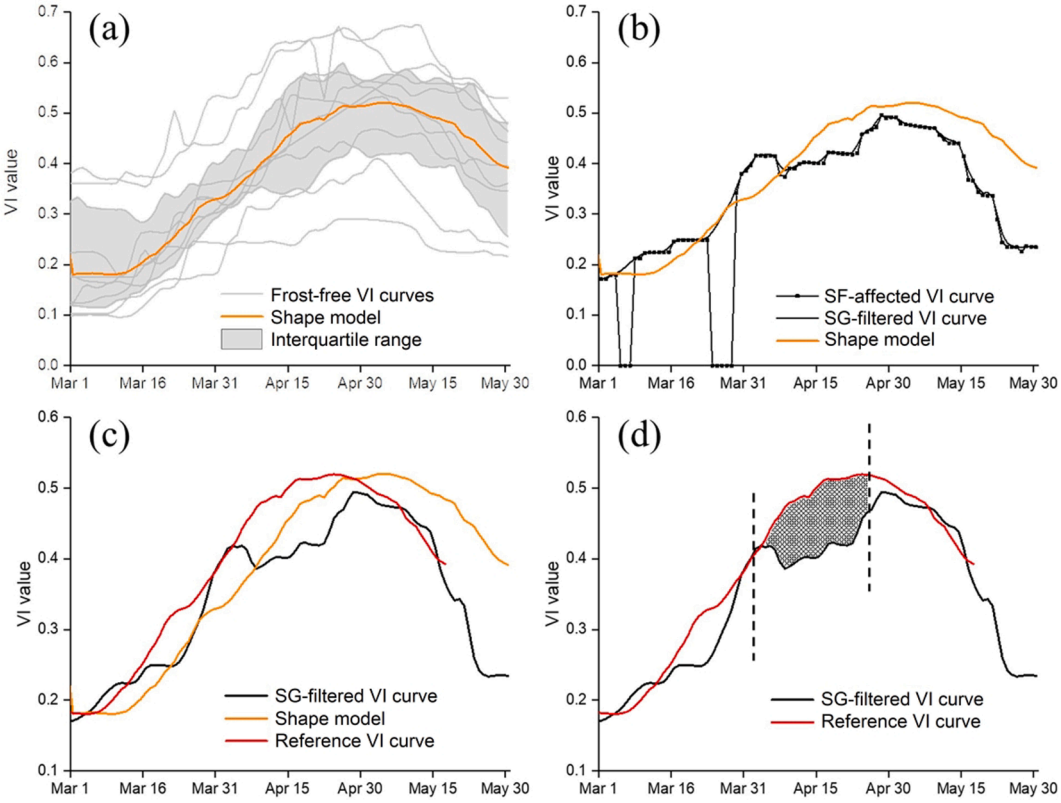

Fig. 2. Schematic of the development of the spring frost damage index (SFDI), in which SF represents the spring frost and SG is the Savitzky-Golay filter. A shape model is defined as the multiyear averaged VI curve. The two black dashed lines represent the start date and end date of the spring frost event impact.

Fig. 2c). $h(x)$ is the reference VI curve transformed from the shape model $g(x)$ by optimizing three scaling parameters, s_x, s_y, and t_0 (red curve in Fig. 2c). Here, s_x and t_0 represent phenological adjustment, while s_y represents magnitude adjustment. The optimal scaling parameters were obtained by minimizing the weighted root mean square error (*wRMSE*, defined in Eq. (5)) between the scaled shape model and the frost-year VI curve using a subroutine named "CONSTRAINED_MIN" (Lasdon et al., 1978; Sakamoto et al., 2010) in the IDL program (ITT Visual Information Solution). The search ranges for each parameter were empirically determined (Sakamoto et al., 2010) as follows: $0.9 < s_x < 1.1$, $0.5 < s_y < 1.85$ and $-10 < t_0 < 10$.

$$wRMSE = \sqrt{\sum_{i=1}^{n} w_i (f(t_i) - h(t_i))^2} \quad (5)$$

In Eq. (5), n is the number of data points in a VI curve, w_i is the weight of the i-th point and t_i is the day-of-year (DOY) for the i-th point. The data points within the frost impacted period were excluded from the optimization process. Different weights were given to each point following Eq. (6) (Chen et al., 2016). In general, the greater the temporal distance D_i between the i-th point t_i and the start point of the frost event t_F, the smaller the weight is.

$$D_i = \begin{cases} 1, t_i = t_F \\ \dfrac{1}{(t_i - t_F)^2}, t_i \neq t_F \end{cases} \quad w_i = \frac{D_i}{\sum_{i=1}^{n} D_i} \quad (6)$$

After applying the SMF method to the multiyear average VI curve, the transformed shape model was obtained, which was finally regarded as the reference VI curve, which is a reasonable representation of the typical growth of winter wheat without the impact of a frost event under comparable climate and cultivation conditions to those of the frost year.

2.1.3. Spring frost damage index (SFDI)

Fig. 2d displays the frost-year VI curve smoothed by the Savitzky-Golay filter and the reference VI curve obtained using the SMF method. Without the spring frost, the VI curve of winter wheat is expected to nearly match the reference VI curve (the red curve in Fig. 2d). However, the frost event imposes a notable impact on the development of winter wheat. As a response, the VI declines dramatically during the frost event, and it usually takes several weeks to return to a relatively normal level due to crop recovery (black curve in Fig. 2d). The area enclosed by these two curves can be considered an indicator reflecting the severity of the frost impact on winter wheat. Accordingly, a remote sensing-based spring frost damage index (SFDI) can be defined as follows:

$$SFDI = \sum_{i=SF_{begin}}^{i=SF_{end}} (VI_{r_i} - VI_{SF_i}) \quad (7)$$

where VI_{r_i} is the value in the reference VI curve, and VI_{SFi} is the value in the spring frost-affected VI curve. SF_{begin} is the start date of the spring frost (marked by the first vertical dashed line in Fig. 2d). SF_{end} is the end date of the SFDI calculation, which can be determined flexibly according to the purpose of the application, such as the end date of the spring frost event observed from the meteorological records or the week after the occurrence of the spring frost event. Accordingly, the SFDI has the potential for near real-time calculation, which makes it possible for farmers to carry out timely field management to reduce frost damage. For the purpose of post assessment of frost damage, the SFDI calculation should include the period of long-lasting impacts from frost damage. In this case, the date when the reference VI curve reached its peak (marked by the second vertical dashed line in Fig. 2d) was carefully set as the end date for the SFDI calculation. The reason for selecting the day with the maximum VI value (before the grouting stage) as the end date was that the signal of spring frost impact was difficult to identify after this date because the grouting stage involves a gradual leaf color change that

creates a confounding VI signal similar to that of the frost impact. In brief, the SFDI was calculated as the area enclosed by the two curves from the start point to the end point and thus considers the continuous impact of spring frost.

2.2. Multiple regression analysis

2.2.1. Linear regression model

Frost damage to winter wheat is affected by many factors (e.g., climatic conditions, cultivation management, and wheat growth status). To screen the respective roles of different factors, multiple linear regression (MLR) analysis was implemented to explore the relationship between the newly developed SFDI and various factors, in which the SFDI and its influential factors were set as explained variables and explanatory variables, respectively. The MLR model can be expressed as follows:

$$SFDI = a_0 + a_1 \cdot x_1 + a_2 \cdot x_2 + a_3 \cdot x_3 + \ldots + a_n \cdot x_n + \varepsilon \quad (8)$$

where a_i is the regression coefficient for factor x_i, and ε is the residual term. To avoid the influence of outliers, Cook's distance was used to judge whether a point was an abnormal point for the explained variable. This judgment was based on the following formula:

$$D > \frac{4}{n-k-1} \quad (9)$$

where D is Cook's distance, n is the number of observations and k is the number of explanatory variables.

2.2.2. Geographically weighted regression

To consider the possibility that the roles of the influential factors were spatially dependent over larger areas, geographically weighted regression (GWR) was also employed to explore the spatial variations in the factor coefficients (Brunsdon et al., 1996; Fotheringham et al.,2003; Charlton and Fotheringham, 2009). The GWR model is given as follows:

$$y_i = \beta_0(u_i, v_i) + \sum_k \beta_k(u_i, v_i) x_{ik} + \varepsilon_i \quad (10)$$

where y_i is the global explained variable (SFDI), x_{ik} is the explanatory variable k (influential factor) at sampling point i, (u_i, v_i) are the spatial coordinates of the i-th sampling point, and $\beta_0(u_i, v_i)$ and $\beta_k(u_i, v_i)$ represent the local coefficients, which can be estimated by considering observations for places near sampling point i as follows:

$$\hat{\beta}(u_i, v_i) = \left(X^T W_i X\right)^{-1} X^T W_i y \quad (11)$$

where

$$W_i = \begin{pmatrix} a_{i1} & 0 & \cdots & 0 \\ 0 & a_{i2} & \cdots & 0 \\ \vdots & \vdots & \ddots & \vdots \\ 0 & 0 & \cdots & a_{iN} \end{pmatrix} \quad (12)$$

and N is the number of observations near point i. W_i is a diagonal weight matrix, which has diagonal elements corresponding to the spatial weight (a_{ij}) when calibrating a weighted regression around point i. The a_{ij} can be determined by spatial weighting functions (also referred to as kernel functions). Here, the Gauss kernel function was used (Eq. (13)) to avoid the estimation error caused by fewer sample data around individual sampling points as follows:

$$a_{ij} = e^{-\frac{1}{2}\left(\frac{d_{ij}}{b}\right)^2} \quad (13)$$

where d_{ij} is the distance between sampling point i and its nearby observation j, and b is a quantity known as the bandwidth. The Akaike information criterion (AIC) was used to determine the optimal bandwidth.

3. Study area and data

3.1. Study area

We chose Henan Province, Shandong Province and the southern part of Hebei Province (110 °E-122 °E and 31 °N-38 °N, Fig. 3) as the case study area. This region is the largest wheat-planting area and has the highest yield in China (Xiao, et al., 2018). This region has a warm temperate climate and favorable environmental conditions for winter wheat cultivation. The annual mean temperature of the study area ranges from 11.0 °C to 15.4 °C from north to south. Climatologically, the lowest monthly average temperature of this area ranges from −4.6 °C to −0.7 °C, which is suitable for growing winter wheat (Jin, 1996). Along the temperature gradient from north to south, the maximum phenological difference of the winter wheat in the study area is approximately one month, with a later wheat growth cycle in the northern area. The annual precipitation of the study area ranges from 520 mm to 980 mm (approximately 280 mm during the wheat growth period), which can meet most of the water demands for the crop. Most of this region is located on the North China Plain, with an average altitude of approximately 200 m. The entire study region falls within a single tile of MODIS imagery (h27v05).

From April 3–7, 2018, a spring frost event occurred in North China with a rapid temperature drop of more than 14 °C, which led to severe frost damage to the winter wheat in the area. This spring frost event can serve as an ideal case for exploring the enduring impact of spring frost on winter wheat and its various influential factors in the natural environment using remotely sensed data. Accordingly, the SFDI was only used for the postdamage assessment in this study.

3.2. Data

The MODIS nadir BRDF-adjusted daily reflectance data (MCD43A4) from 2001 to 2018 were downloaded from the NASA EARTHDATA website (https://earthdata.nasa.gov/). The original MCD43A4 data were produced on a sinusoidal tile grid in the HDF-EOS format (with a resolution of approximately 500 m), and they were reprojected into the GCS_WGS_1984 coordinate system in GeoTIFF format by the official HDF-EOS to GeoTIFF conversion tool (HEG). Considering that the frost event occurred in April 2018, only the data between March 1 and May 31 were used to generate VI data (i.e., NDVI, EVI and NDPI). The VI data of the years from 2001 to 2017 without severe frost events were used to calculate the multiyear average VI curve as the shape model. The reference VI curve was then derived by adjusting the shape model to match the VI curve of 2018 following the method described in Section 2.1.2. Then, the SFDI was calculated for the spring frost event that occurred from April 3–7, 2018. Since the duration of a spring frost is usually no longer than a week, we used the daily MODIS reflectance to calculate VI data instead of using multiday composite data (e.g., 8 days or 16 days) in this study. The multiday composite data selected a value with the best quality to represent the value over a certain time interval (8–16 days) to minimize the influences of external factors, such as cloud and atmospheric conditions, on the remotely sensed data (Holben, 1986; van Leeuwen et al., 1999). However, composite data can still suffer from remaining noise from atmospheric conditions (Ql and Kerr, 1997) and lose important temporal information caused by the compositing process, which is useful for detecting abrupt change. For example, if the peak date of a frost event is not selected during the compositing process, the signal represented in the VI data would be weakened by the use of the multiday composite data. Moreover, if the frost impact period was shorter than the composite period (8–16 days), the signal of the frost impact might be ignored by the compositing process (Ql and Kerr, 1997). The BRDF-adjusted daily reflectance data allowed us to analyze the detailed signal of the winter wheat response to spring frost and avoid

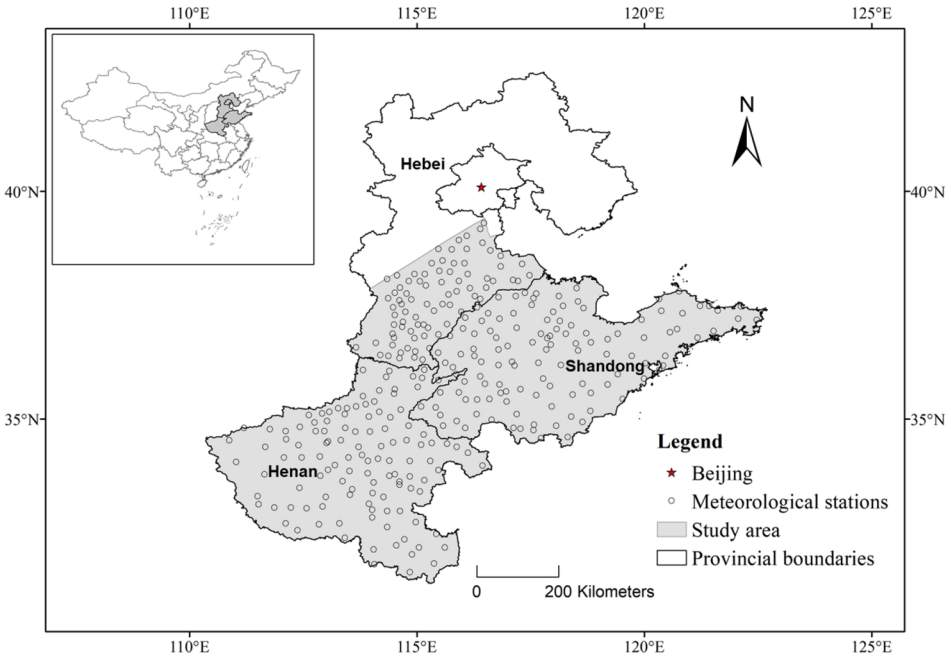

Fig. 3. The study area and locations of meteorological stations.

losing (or weakening) the frost event signal during the VI compositing process. To remove the VI data noise caused by cloud contamination and poor atmospheric conditions, the daily VI data calculated from MCD43A4 were smoothed by the Savitzky-Golay (SG) filter (Chen et al., 2004). Moreover, we kept only the pixels within the winter wheat cultivation area for subsequent analysis, which were identified using a 16-meter crop type map provided by the Chinese Academy of Agricultural Sciences (CAAS) (Tang et al., 2016).

In addition, the daily meteorological data (2001–2018) of 319 meteorological stations located in the study area (Fig. 3) were collected from the Chinese Meteorological Administration (CMA) and included the mean temperature, minimum temperature, and precipitation. The meteorological data were used to identify frost-free years based on the method described in the China National Standard (Standardization Administration, 2017), to determine the start date of the frost event and to calculate the meteorological factors for the frost year.

Additionally, daily soil moisture data from 2018 were acquired from the ESA Soil Moisture Climate Change Initiative (CCI) project (Gruber et al., 2017; Dorigo et al., 2017; Gruber et al., 2019), which provides spatially complete and temporally consistent global soil moisture data at a spatial resolution of 0.25° by merging both active and passive microwave satellite sensor data (https://www.esa-soilmoisture-cci.org/).

Finally, county-level wheat yield data from 2014 to 2018 in Henan Province and Shandong Province were collected from the EPS CHINA DATA platform (http://olap.epsnet.com.cn/) to evaluate the effectiveness of SFDI on quantifying spring frost damage. Unfortunately, there were no relevant data for Hebei Province for 2018; thus, Hebei was excluded from the validation analysis.

3.3. Factors influencing spring frost damage

Previous studies have shown that the severity of winter wheat damage from spring frost is mainly controlled by environmental factors (e.g., temperature and soil moisture) and crop growth conditions (Kang et al., 2002; Rozbicki et al., 2015; Sun et al., 2018). Accordingly, factors related to crop growth and environmental conditions were calculated from the collected data to explain the spatial variation in the SFDI across the study area. The detailed definitions of the factors and how to calculate the factors are explained below.

3.3.1. Factors related to crop growth conditions

Since spring frost damage can be affected by crop growth conditions, five factors were selected according to existing studies (Gu et al., 2008; Eccel et al., 2009; Zheng et al., 2015): sowing date (SD), green-up date (GUD), maximum VI value during the tillering stage (VI_{til}), VI value at green-up date (VI_{gud}) and VI value before the occurrence of the frost event (VI_{bsf}) (shown in Fig. 4a). The first two factors represent the phenological status, while the remaining factors represent the crop growth status at the corresponding phenological stages. Generally, early sowing and green-up dates indicate that the crop is at an advanced phenological stage. The VI value before the frost event reflects the crop condition resulting from both the growth status and the phenological stage before the frost event. A higher VI_{bsf} value indicates that the crop may have greater vulnerability to spring frost.

Most of these factors, except the sowing date, can be directly obtained from the remotely sensed VI curve. It is difficult to collect the sowing date for a large area in the field. Considering the link between the sowing date and the VI curve, we indirectly estimated the sowing date by calculating the date when the VI value achieved the 50% threshold of the first small peak (Til_{50}) in the VI curve, which corresponds to the maximum VI during the tillering stage. This estimation was reasonable and acceptable because an early Til_{50} corresponds to an early sowing date under typical conditions. Moreover, the GUD was determined using the logistic method (Zhang et al., 2003), in which the GUD was defined as the date when the change rate of the curvature of the logistic-fitted VI curve reached its first local maximum.

After extracting these five factors (Til_{50}, GUD, VI_{til}, VI_{gud} and VI_{bsf}), it is necessary to reduce the geographical differences in both the crop growth cycle and the growth conditions across the large study area via standardization. Based on the five factors derived from the VI curves of all frost-free years, we calculated the pixel-based interquartile average of all values falling between the upper and lower quartiles. The pixel-based interquartile averages were then subtracted from the values of the five factors obtained in the spring frost year. Taking VI_{bsf} as an example, the formula to standardize the geographical differences can be expressed as follows:

$$VI_{bsf-s} = VI_{bsf} - \overline{VI_{bsf}} \tag{14}$$

where $\overline{VI_{bsf}}$ and VI_{bsf-s} are the interquartile average and standardized

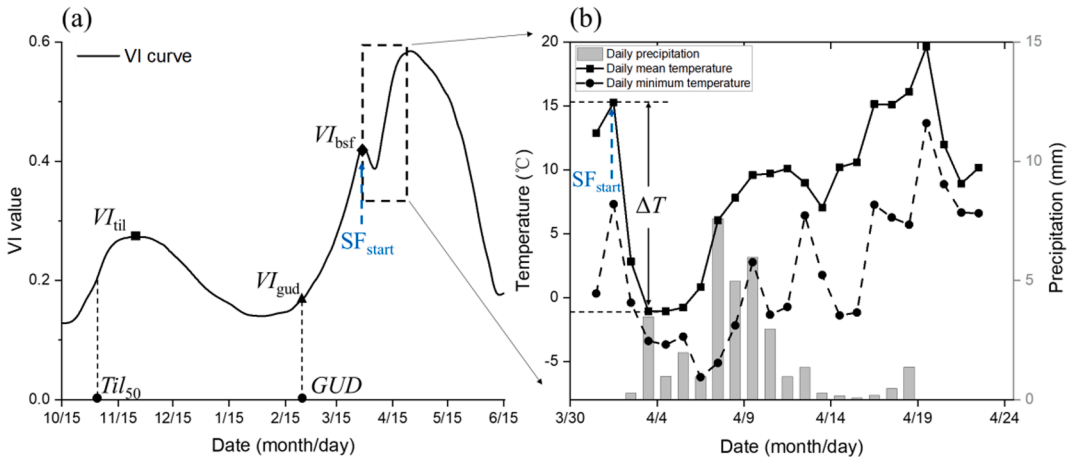

Fig. 4. Definitions of five factors related to crop growth conditions (a) and environment-related factors (b). The blue arrow represents the start date of spring frost.

values for the VI_{bsf} factor, respectively. The standardization of the other four factors was similar. After standardization, the values of the five factors represented the changes in the spring frost year compared with the averaged conditions without spring frost, which ensured that the factor values for all pixels were comparable over a larger area.

3.3.2. Factors related to environmental conditions

Frost damage is supposed to be inversely proportional to the freezing temperature and proportional to the duration of the freezing days (Cannell and Smith, 1986). Therefore, the accumulated frost degree-days (*AFDD*), which is defined as accumulated days when the temperature is below a given threshold (T_{thr}) during the frost event, was used to represent the comprehensive effects of the intensity and duration of the event (Eq. (15) (Xiao et al., 2018). This metric can be calculated from both the daily mean temperature ($AFDD_{mean}$) and the daily minimum temperature ($AFDD_{min}$) with thresholds (T_{thr}) of 10 °C and 2 °C, respectively. The temperature thresholds were chosen to be consistent with those of previous studies (Li et al., 2010; Crimp et al., 2015; Xiao et al., 2018). To further reflect the spring frost intensity, the temperature drop range (ΔT) was also calculated as the difference between the daily mean temperature at the beginning of the frost event and the minimum of the daily mean temperature across the frost period (Eq. (16)) (Ma et al., 2011). In addition, the total precipitation (P_t) during the frost impact period was also selected to reflect the water conditions under low temperature stress (Eq. (17)).

$$AFDD_{var} = \sum_{i=SF_{start}}^{i=SF_{end}} \max\left(T_{thr} - T_{var}^{i}, 0\right) \tag{15}$$

$$\Delta T = T_{start} - T_{min} \tag{16}$$

$$P_t = \sum_{i=SF_{start}}^{i=SF_{end}} P_i \tag{17}$$

The subscript *var* can be set as the *mean* or min, which correspond to the daily mean temperature or daily minimum temperature. T_{start} is the daily mean temperature at the beginning of the frost event, and T_{min} is the minimum daily mean temperature during the frost period (Fig. 4b). These abovementioned factors were calculated for each meteorological station and then interpolated by the kriging method to the MODIS grid.

Some studies have shown that irrigation before frost events can greatly alleviate the damage to winter wheat (Kang et al., 2002; Meng et al., 2017); thus, soil moisture (SM) at the beginning of the frost event was also used as a proxy for irrigation status for the crop. The main problem here is that the ESA Soil Moisture CCI data have a coarser spatial resolution than MODIS. Accordingly, a thin plate spline (TPS) function was used to interpolate the soil moisture data to 500-m resolution (Dubrule, 1984; Zhu et al., 2016).

4. Results

4.1. Spatial distribution of SFDI

Based on the method proposed above, three VIs were used to calculate the SFDI that quantified the VI response of winter wheat to the spring frost event (Fig. 5a, c, and e). Overall, the SFDI values calculated from the three VIs had similar spatial patterns, and their spatial correlation exceeded 0.8. This suggests that all three VIs can capture similar impacts of the spring frost. The distributions of their histograms were also similar (Fig. 5a, c, and e). The severely impacted areas with higher SFDI values were mainly located at the junction of Hebei, Henan and Shandong provinces, especially in the western part of Shandong Province. The frost impact degraded as the frost moved away from the serving affected area. Since all three VI-based SFDI showed similar patterns of spring frost impact, only $SFDI_{ndpi}$ was used in the following analysis because of its advantages of removing the snow background noise, containing more information than $SFDI_{ndvi}$ and $SFDI_{evi}$ and having a higher mean and variance (mean: 0.74 *v.s.* 0.69, 0.69; variance: 0.50 *v.s.* 0.46, 0.39). Additionally, we also calculated the VI differences (ΔVI) between the spring frost year and the previous frost-free year (Fig. 5b, d, and f) to compare with the SFDI results in Fig. 5a, c and e. The spatial distribution of the VI differences showed large variations across the study area with contrasting signs. Some areas even experienced an increase in VI during the frost event, which suggests that the spring frost event benefited the crops in these regions (Fig. 5b, d, and f). This confusing signal was likely caused by the yearly variation in weather conditions and other environmental factors. The SFDI did not suffer from such variation and showed a more cohesive spatial pattern of frost damage to winter wheat (Fig. 5a, c, and e).

To validate the spatial distribution of the SFDI in the absence of actual frost damage data, we collected reports from several regional newspapers in the three provinces in 2018 based on keywords (Fig. 5g). These printed newspapers were retrieved from the National Library of China and included Henan Daily and the rural edition of Henan Daily in Henan Province; Dazhong Daily and the rural edition of Dazhong Daily in Shandong Province; and Hebei Daily, Hebei Farmers' Newspaper, and Yanzhao Metropolis Daily in Hebei Province. Assuming that frost-stricken areas are more likely to be reported in newspapers than in less affected areas, the frequency of local region names that appeared in the frost-related newspaper reports can be used to identify regions that were seriously or slightly affected by a frost event. For unreported areas, we assumed that the impact of spring frost was very limited. This kind of validation is qualitative and may not be accurate, but it can test the rationality of the spatial pattern of our results to a certain extent. The results of the frost keyword retrieval showed that several counties

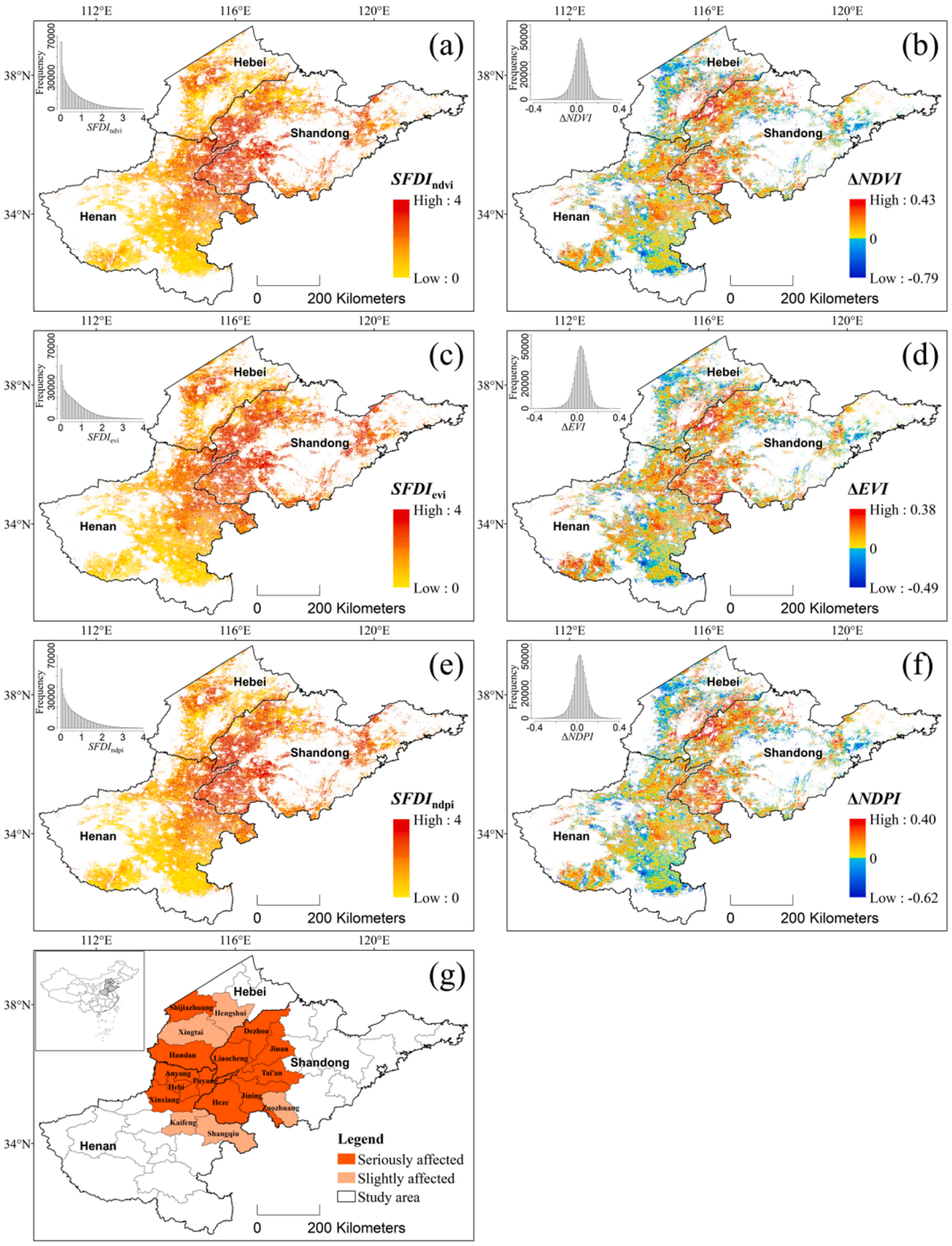

Fig. 5. Spatial distribution of NDVI-based SFDI (a), ΔNDVI (b), EVI-based SFDI (c), ΔEVI (d), NDPI-based SFDI (e), ΔNDPI (f), and hotspots derived from newspaper keywords (g). The subgraphs in (a)-(f) are their respective histogram distributions. The subgraph in (g) is the location of the study area in China.

located at the junction of Hebei, Henan and Shandong provinces were seriously affected (red in Fig. 5g) or slightly affected by frost events (light orange in Fig. 5g), while the rest of the study area was not considered to be affected by the frost event. Such a spatial pattern is generally consistent with the SFDI pattern shown in Fig. 5a, c, and e. In addition, city-level research on the meteorological conditions of the winter wheat growth period found that the same frost event imposed slight freezing damage to winter wheat in Shangqiu city in April 2018 (Shi, 2019), which was also consistent with our results. All of these results indicated that the SFDI is suitable and effective for mapping the frost impact on winter wheat at the provincial scale.

Furthermore, we also used county-level winter wheat yield data in 2018 to validate the effectiveness of SFDI in reflecting the crop yield decline due to the spring frost event (Xiao et al., 2018; Nuttall et al., 2019). The yield anomaly (Δ*Yield*) was calculated by subtracting the average crop yield of frost-free years during the past five years (i.e., 2014, 2016 and 2017) from the wheat yield of 2018. The scatterplot between the yield anomaly and SFDI at the county level is shown in Fig. 6 along with the linear and logarithmic model fitting (Table 1). Compared to the average yield of the frost-free years, the county-level yield in the frost-affected years (2018) decreased with the increase in the SFDI. Both fitting models show that the Δ*Yield* was significantly negatively related to the SFDI ($p < 0.01$ in the linear model and $p < 0.001$ in the logarithmic model, Fig. 6). However, the R^2 was relatively

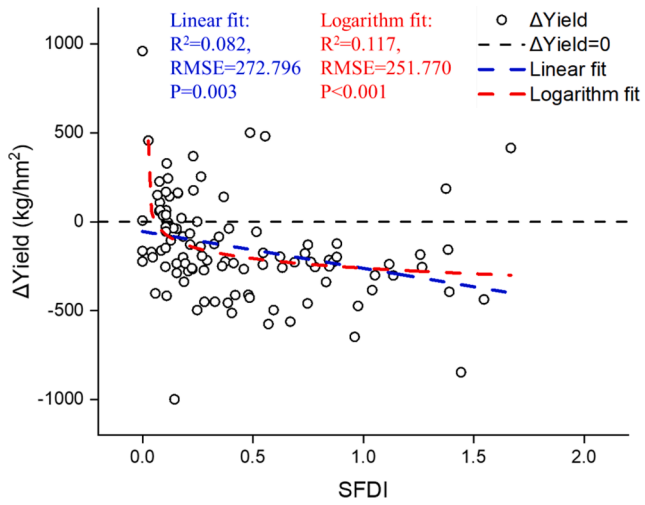

Fig. 6. Scatterplot between the yield anomaly and the SFDI in 2018.

Table 1
Fitting coefficients between the yield anomaly and the SFDI.

Fitting methods	Parameters	Value	t-Value	Prob>|t|
Linear	Intercept	−73.014	−1.836	0.069
	Slope	−184.979	−2.997	0.003
Logarithm	a	−281.171	−7.017	0.000
	b	90.713	1.743	0.085
	c	−0.014	−0.135	0.893

low despite the statistically significant association between the SFDI and yield anomaly. One potential reason for the smaller R^2 was that the environmental conditions and field management measures after the frost might have offset the damage to the crop yield caused by the frost. Without proper field survey data, it is difficult to distinguish the direct contribution of the frost event from the final yield. Nevertheless, the result of winter wheat yield analysis at the county level showed that the SFDI can reasonably reflect the damage caused by spring frost events to a certain extent.

4.2. MLR model analysis

To understand which factors might strongly influence SFDI, stepwise multiple linear regression was used to identify high-impact explanatory variables from the pool of all candidate factors. Only variables with significant contributions to explain the SFDI information were retained. As a result, four factors were retained in the MLR model, including the standardized VI value ($VI_{bsf\text{-}s}$), soil moisture (*SM*) before the frost event, accumulated frost degree-days calculated from the daily mean temperature ($AFDD_{mean}$), and total precipitation during the spring frost period (P_t). Table 2 shows the coefficient and variance inflation factor (VIF) of each factor in the final MLR model. All VIF values were close to 1, indicating that multicollinearity did not exist among the selected factors (Mansfield and Helms, 1982; Daoud, 2017). *SM* and P_t were significantly negatively correlated with the SFDI, while the other two factors were significantly positively correlated with the SFDI (all p values < 0.001). The negative coefficients indicated that good water availability (more soil moisture before the spring frost event and more precipitation during the spring frost period) may alleviate frost damage to winter wheat. On the other hand, higher values of $VI_{bsf\text{-}s}$ and $AFDD_{mean}$ can be associated with more severe frost damage. The standardized coefficients in Table 2 indicate that $VI_{bsf\text{-}s}$ and P_t were more influential factors. The scatterplot of the observed SFDI and predicted SFDI in the MLR model is shown in Fig. 7a with R^2 equal to 0.362 and RMSE equal to 0.532 ($n = 551{,}564$, $p < 0.001$).

Table 2
Multiple linear regression coefficients.

Variables	Unstandardized Coefficients	Standardized Coefficients	*t*-value	Sig.	VIF
(Constant)	0.734		151.748	0.000	
$VI_{bsf\text{-}s}$	3.203	0.433	398.138	0.000	1.024
SM	−1.637	−0.118	−102.158	0.000	1.150
$AFDD_{mean}$	0.016	0.142	94.083	0.000	1.966
P_t	−0.005	−0.245	−170.216	0.000	1.791

4.3. GWR model analysis

GWR was implemented to examine whether there was spatial nonstationarity in the relationship between the SFDI and the selected four factors. To make the coefficients comparable, the standardized *z* score of the factors was used for GWR. Fig. 7b shows the scatterplot between the observed SFDI and predicted SFDI in the GWR model. Overall, the GWR model demonstrated better performance than MLR, with higher global R^2 (0.479 *v.s.* 0.362) and smaller RMSE (0.443 *v.s.* 0.532). More importantly, the GWR model showed more uniform performance for different SFDI ranges after considering the spatial nonstationarity, with less severe underestimation/overestimation for high/low SFDI values (Fig. 7).

Fig. 8(a, b) presents the variation in the local R^2 and the predicted standard error across the study area in the GWR model. This result revealed that the GWR model was more effective over the area that was seriously affected by the spring frost event (Fig. 5), indicating that the SFDI was better associated with these factors over severe frost impacted regions. The prediction errors in these areas were also relatively small in comparison with those in the other areas (Fig. 8b). Fig. 8(c-f) presents the local regression coefficients for each explanatory factor in the GWR model. The negative associations are shown by cold colors, while the positive associations are indicated by warm colors. The relationships between the SFDI and the four explanatory factors showed substantial variations across the study area, while some regions showed inconsistent results with the MLR model. The coefficients for $VI_{bsf\text{-}s}$ of the entire study area were all positive, with high values appearing over western Shandong Province (Fig. 8c). The coefficients of P_{total} in most parts of the study area were negative (Fig. 8f). The relationship between these two factors and SFDI were almost identical to the results of the MLR model (Table 2) and had various regional differences. This confirmed that high values of $VI_{bsf\text{-}s}$ can aggravate frost damage, while abundant precipitation can alleviate this damage. On the other hand, the local regression coefficients of soil moisture (*SM*) and accumulated frost degree-days ($AFDD_{mean}$) displayed more diverse spatial patterns. These two factors were positively associated with the SFDI in some places but negatively affected the SFDI in other areas (Fig. 8d, e). This divergent spatial pattern affirmed the MLR results that *SM* and $AFDD_{mean}$ were likely secondary factors in influencing the SFDI.

5. Discussion

5.1. Advantages and limitations of SFDI

Vegetation indexes calculated from remotely sensed data are commonly used as indicators of vegetation greenness and vigor (Huete et al., 2002; Prasad et al., 2005). Previous studies have shown that frost-induced damage to vegetation can be identified by reduced VI values (Gu et al., 2008; Menzel et al., 2015; Bascietto et al., 2018; Allevato et al. 2019). The physiological mechanism of the decline in VI due to frost has been reported by several existing studies (Guy, 1990; Wang et al., 2012; Wei et al., 2017). During the frozen and post-thawing periods, the decomposition of pigments is greater than the composition; thus, the leaf chlorophyll content is decreased significantly. The change in chlorophyll content can slightly increase the reflection of red wavelengths

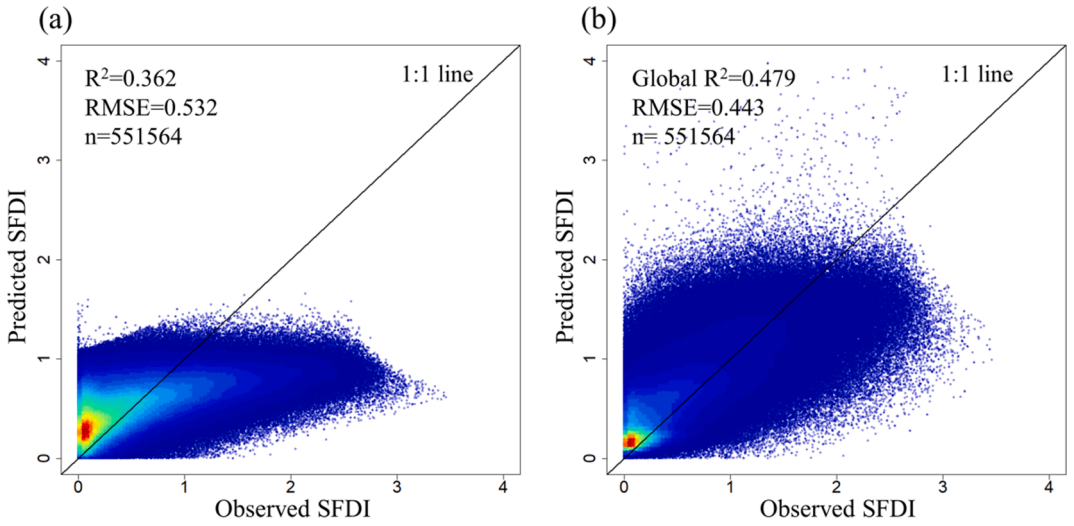

Fig. 7. Scatterplots of observed SFDI values *vs.* predicted SFDI values by the MLR model (a) and GWR model (b). The depth of color represents the density of the data point distribution. The red color represents a higher density of the data points.

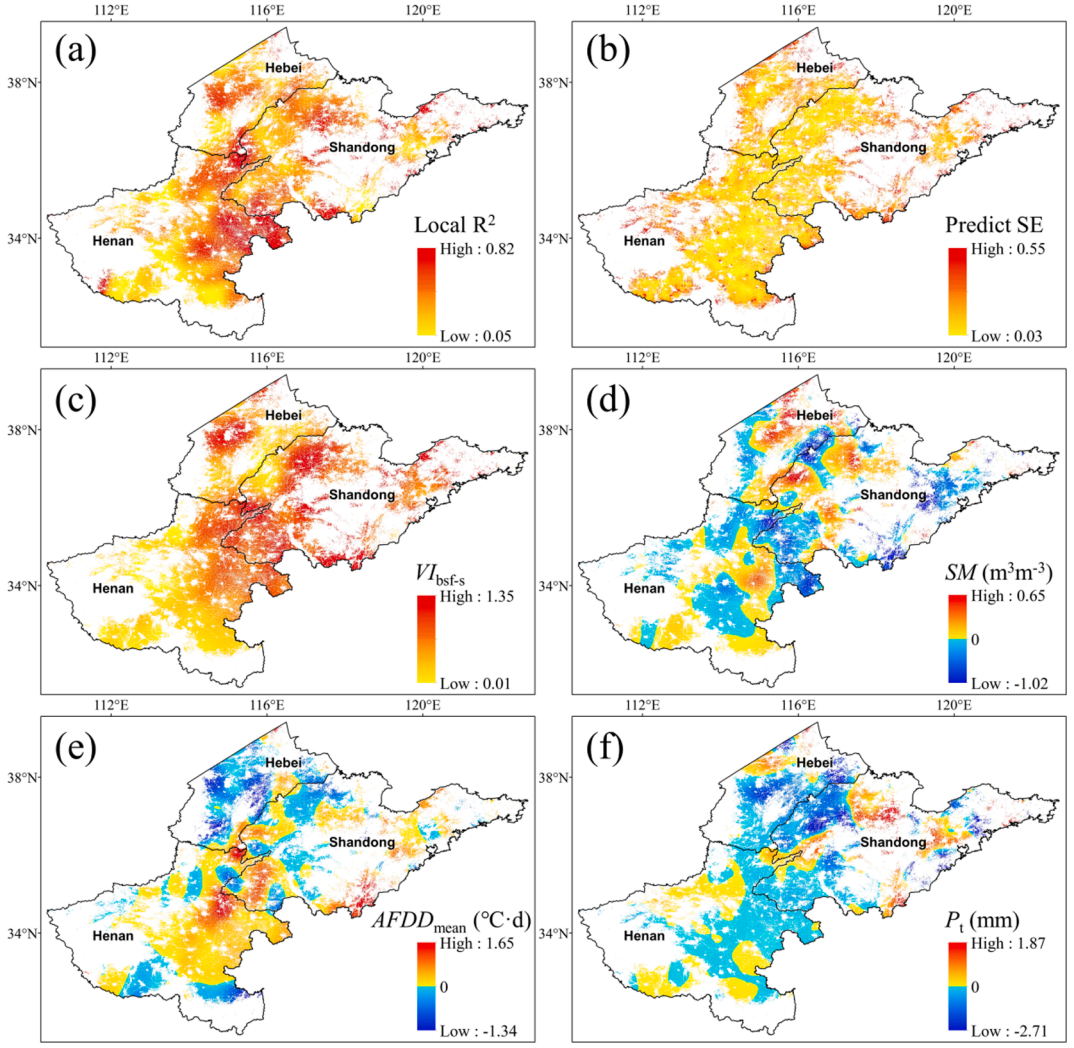

Fig. 8. Distribution of local R^2 (a), predicted standard error (b) and local coefficients for selected factors in the GWR model (c-f).

while decreasing the reflection of green wavelengths. Meanwhile, ice crystals form between cells, and the gradient of water potential between the inside and the outside of cells can lead to cellular dehydration and cell collapse. Consequently, the reflection of the NIR wavelength decreases because of the changing cell structure, while the water absorption valley in the SWIR wavelength weakens due to the reduction in leaf water content. These changes in vegetation spectral characteristics lead to obvious changes in the calculated VI. The increasing red reflectance and decreasing NIR reflectance consequently lead to a notable reduction in the NDVI and EVI values for winter wheat under frost stress. The NDPI replaces the red band with the weighted sum of the reflectance of red and SWIR bands (red-SWIR reflectance, Wang et al., 2017). As the reflectances of both the red and SWIR bands increased under frost stress, the value of the NDPI also decreased substantially, which was similar to the responses of the NDVI and EVI to frost damage. The factors that led to a more significant response of the NDPI to frost damage than the NDVI and EVI (Fig. 5) may come from two advantages of the NDPI. First, the NDPI is sensitive to cell water content because it includes the water-sensitive SWIR band. Second, the NDPI greatly enhances the signal contrast between vegetation and background (e.g., soil and snow) and minimizes the background difference over a large area (Wang et al., 2017, Chen et al., 2019). Therefore, the NDPI appeared to be more suitable for monitoring frost damage to winter wheat.

In previous studies, the difference in the VI between the frost-affected year and a historical frost-free year was commonly used to identify and evaluate frost damage (Nolè et al., 2018; Allevato, et al., 2019). Additionally, the drop in the VI after a frost event compared to prefrost conditions has also been used to identify frost damage (Menzel et al., 2015). For the first method that selects a single frost-free year as a reference, the difference in VI between the frost year and frost-free year may result from both frost damage and the differences in climatic conditions and phenology between the two years. It is not trivial to separate the impact of frost from other confounding factors due to a lack of interannual correction. For the second method of using VI reduction before and after the frost event, it is difficult to locate the exact date that represents the occurrence of the most severe frost injury. Although the minimum VI following a frost event is typically used, the minimum VI value can potentially be caused by cloud contamination. More importantly, these two types of methods both regard spring frost as a short-term event and ignore the continuous impact of spring frost on the crop. To address these issues, the SFDI considers both the immediate VI reduction when frost occurs and the continuous impact of frost on crops during the crop recovery period. The SFDI calculates the cumulative VI reduction between the reference VI curve and the frost-affected VI curve (Fig. 2) during the entire recovery period, which is more robust against cloud contamination on an individual date and includes the continuous impact of spring frost. In the construction of the SFDI, the selection of a reference VI curve that represents the actual trajectory of crop growth under frost-free conditions is of great importance. The multiyear average VI curve from frost-free years was used as the candidate reference curve, which can make the reference curve more stable compared with using a single VI curve or fewer frost-free VI curves. Moreover, to reduce interannual variations caused by changes in farmers' cultivation practices and in climatic conditions, the multiyear average VI curve was further geometrically scaled by the shape model fitting (SMF) method to match the actual trajectory of crop growth under frost-free conditions in the year of interest. The SMF method was verified to be effective in simultaneously eliminating phenological shifts and changes in VI magnitudes (Sakamoto et al.; 2010, 2013, Sakamoto, 2018) through three optimized scaling parameters (s_x, s_y, t_0). To optimize these parameters, we used *wRMSE* instead of the original *RMSE* because it can ensure better consistency between the reference VI curve and the frost year VI curve by assigning higher weight to dates closer to the date when the spring frost event occurred. This modification greatly reduced the uncertainty in SFDI calculations caused by interannual differences in the VI curves.

Due to the lack of proper fieldwork and survey data on the actual frost damage to winter wheat that occurred in the past, it was very challenging to validate our SFDI results directly. To overcome this challenge, we used regional newspaper reports of the event and county-level winter wheat yield data as proxies to assess the performance of the SFDI indirectly. To address this issue, future work to collect proper field data during spring frost events is needed. Such data can be used to further evaluate the effectiveness of the SFDI, and provide unique value for the broad community who are interested in using remotely sensed data to study spring frost damage. With the rapid development of citizen science and volunteered geographic information systems on mobile devices, we are planning to explore the possibility of using such technologies to crowdsource field data at county-to-provincial scale.

The proposed SFDI represents a step forward in automatically detecting areas subject to spring frost impacts and quantifying the intensity of frost damage at the provincial scale by using remotely sensed VI time series. Although the SFDI was applied to data at the provincial scale, it is very flexible and can be easily extended to continental and global data. Three advantages of the SFDI can be summarized as follows: (1) the SFDI is easy to implement using widely available VI time-series datasets; (2) the SFDI is calculated as the area enclosed by the two curves from the start point to the end point. The end point can be set flexibly according to the purpose of the application, which can be used for near real-time or continuous spring frost impact assessment; and (3) the methodology can be easily extended to other natural hazards and other crop types with reasonable adjustment.

The newly proposed SFDI also has limitations due to several necessary assumptions made during its calculation. Previous studies have revealed that a frost event can inevitably lead to a decline in VI values (Gu et al., 2008; Menzel et al., 2015; Bascietto et al., 2018; Allevato et al. 2019). However, other agricultural events (e.g., drought, diseases, and pests) may also reduce VI values. Thus, it is difficult to isolate the proportion of the VI declines resulting from a frost event without prior knowledge or assumptions. Therefore, the SFDI requires prior knowledge of the frost event and its start date from the meteorological record or forecast. Moreover, if the period used for SFDI calculation coincides with other agricultural events or another spring frost, the SFDI reflects the compounding impacts rather than the independent impact of the frost event of interest. It is difficult to isolate individual contributions from different events to SFDI unless a more reasonable end date can be identified from the physiological mechanism in future studies. Additionally, the SFDI is recommended for assessing the frost damage for a single crop type (e.g., winter wheat) rather than for multiple crop types simultaneously because different crop growth cycles can offset the signals among different crop types, and making the SFDI values incomparable.

Moreover, we used daily MODIS products at the 500-m resolution for the case study. Although the method itself is not dependent on the spatial resolution of remotely sensed data, it should be noted that medium resolution data like MODIS may not be suitable for monitoring small plantations (less than 25–100 ha). To apply SFDI for small cultivated areas, higher spatial resolution data, such as Sentinel-2, Landsat, Planet, and WorldView, are needed. Theoretically, the monitoring results using higher spatial resolution data would not differ much from our 500-m resolution monitoring results since the method is not resolution-dependent. There may be slight differences in the spatial patterns as higher resolution data may reveal more spatial details. It should be noted that high spatial resolution data typically do not provide frequent revisit time which is also essential for this type of rapid response and monitoring. One would argue the increasing number of high-resolution satellite sensors and constellation may fill in the temporal gap. But cautions need to be taken to ensure the data consistency when using data from different platforms for monitoring and rapid response. One potential solution to address the issue of spatial–temporal resolution tradeoff is to apply data blending methods (e.g., STARFM, FSDAF, etc.) (Gao et al., 2006; Zhu et al., 2016).

5.2. Main factors influencing the SFDI distribution

According to existing studies, ten factors associated with biotic and abiotic conditions were selected to establish the regression model between the SFDI and the related factors. The model was expected to explain the spatial variation in the SFDI. As a result of stepwise multivariate linear regression, only four factors were retained in the model, including $VI_{bsf\text{-}s}$, *SM*, $AFDD_{mean}$, and P_t. The first factor represents the growth condition of the winter wheat crop, and the other three factors describe abiotic conditions. This indicates that the interaction among biotic and abiotic factors can determine the spatial pattern of the SFDI, which is consistent with existing studies (Menzel et al., 2015; Meng et al., 2017; Zheng et al., 2018). Among all biotic factors, the sowing date (*SD*), green-up date (*GUD*), and VI_{gud}, representing crop phenology and growth status in the winter and early spring, respectively, were not included in the model. The exclusion of these biotic factors seems to conflict with previous studies, which suggested that earlier sowing dates and green-up dates tended to increase the vulnerability to spring frost (Zhao et al., 2014; Liu et al., 2018). This may be due to the relatively long time interval between the sowing time (or green-up) and spring frost. In contrast, a new factor ($VI_{bsf\text{-}s}$) representing growth status close to the frost event was chosen by the model because it represents the combined effect of crop phenology and growth conditions after green-up. Higher values of $VI_{bsf\text{-}s}$ indicate that the crop is at a more vulnerable stage to low temperatures when spring frost occurs. Theoretically, winter wheat is at the stem elongation or jointing stage when it resumes growth in spring. This stage is critical for spikelet differentiation and is very sensitive to temperature changes. If a severe spring frost were to occur during this period, spikelet differentiation would stop, and the seed setting rate would also decrease. Furthermore, during the process of spikelet differentiation, the crop's resistance to low temperature decreases rapidly; thus, winter wheat becomes more susceptible to frost events (Frederiks et al., 2012; Li et al., 2015; Xiao et al., 2018).

Among the abiotic factors, the accumulated frost degree days ($AFDD_{mean}$) was retained in the regression model rather than the temperature drop range (ΔT) because both freezing temperature and the duration of freezing days were important in determining the level of frost damage (Cannell and Smith, 1986; Xiao et al., 2018). Additionally, *SM* and P_t, which reflect the water abundance before and after spring frost, respectively, were both retained in the regression model. This suggests that the water condition is a key factor that may affect the severity of spring frost damage to winter wheat, which is consistent with existing studies (Wang et al., 2012; Zhao et al., 2014; Meng et al., 2017). One plausible reason is that moist soil has more heat capacity and can absorb more heat, serving as a heat sink and releasing heat to the near-surface atmosphere, thus reducing the frost impact (Burke et al., 1976;

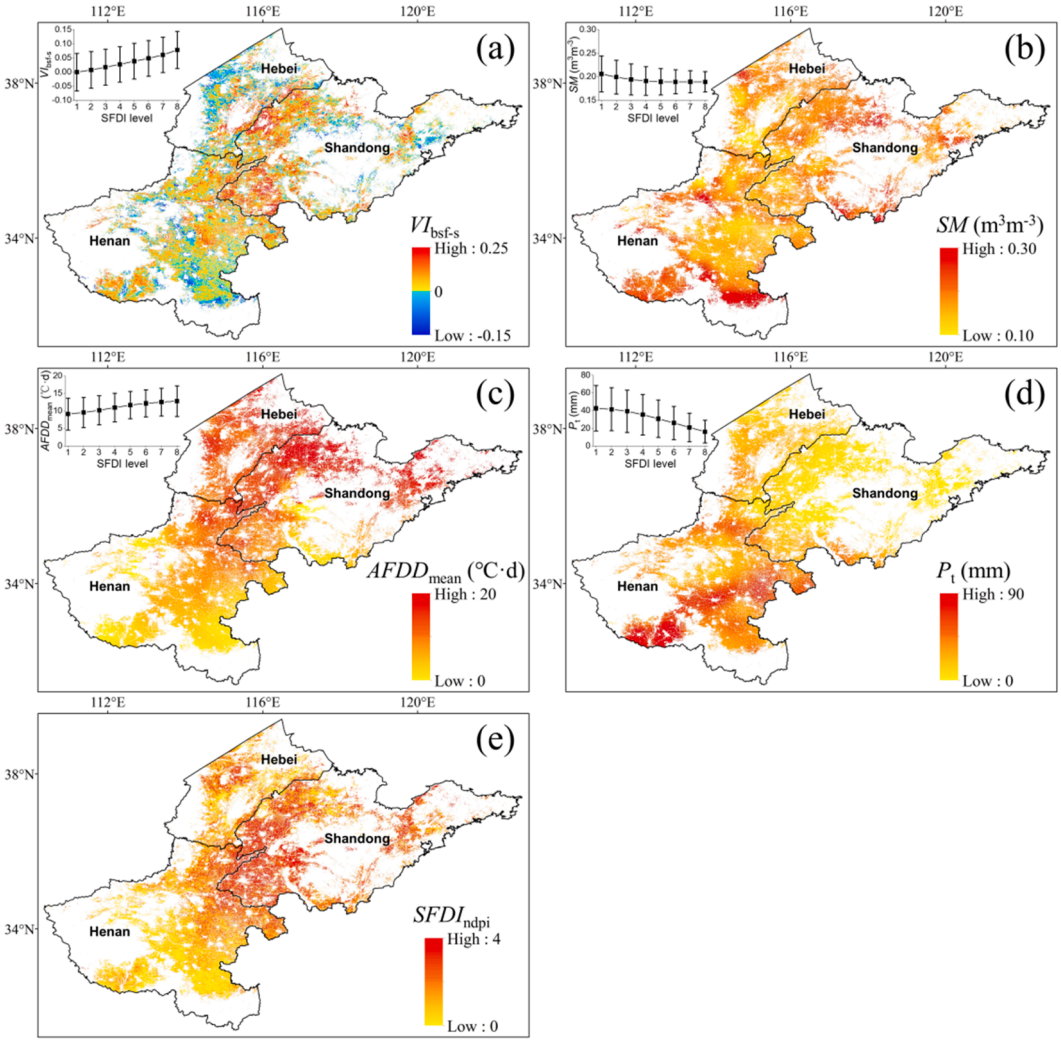

Fig. 9. Spatial distribution of selected factors (a-d) and NDPI-based SFDI (e). The upper left subgraphs in Fig. 9a-d show the relationship between each factor and the SFDI in eight groups, and the labels on the horizontal axis represent different levels of SFDI. The black solid squares in the graph represent the mean values of different factors for each group. Error bars represent the mean ± standard deviation for each group.

Klein et al., 1994; Trought et al., 1999; Snyder and de Melo-Abreu, 2005).

Fig. 9 shows the spatial distribution of $SFDI_{ndpi}$ (Fig. 9e) and four retained factors (Fig. 9a-d). It was clear that for most of the study area, the $VI_{bsf\text{-}s}$ values were positive, indicating increased VI_{bsf} values in 2018 compared to in the previous frost-free years (Fig. 9a). Soil moisture displayed relatively small values except for in the southern part of the study area (Fig. 9b). The accumulated frost degree-days ($AFDD_{mean}$) showed a decreasing trend from north to south, with values exceeding 10 ℃·days in most of the area (Fig. 9c). In contrast, the precipitation generally displayed an increasing trend from north to south. More abundant precipitation was observed in Henan Province, followed by Hebei Province and Shandong Province (Fig. 9d). To reflect the relationship between the SFDI and four selected factors more intuitively, we divided the SFDI into eight groups from low value to high value and calculated the mean and standard deviation of four factors corresponding to each SFDI group (the upper left subgraphs in Fig. 9a-d). The results clearly showed that SFDI was positively associated with $VI_{bsf\text{-}s}$ and $AFDD_{mean}$ but negatively associated with SM and P_{total}. Analysis of the variance among the different SFDI values revealed that the differences between groups were significant ($p < 0.001$). These relationships were consistent with the results of the MLR model, as summarized in Table 2.

The roles of the abovementioned factors in deciding the damage to winter wheat can partially explain the spatial distribution of the SFDI, which was more severe at the junction of Henan, Hebei, and Shandong, especially in western Shandong Province (Fig. 9e). Western Shandong Province had relatively higher VI values before the spring frost (VI_{bsf}) than those in Hebei Province but lower VI values than those in Henan Province. On the one hand, the accumulated frost degree-days ($AFDD_{mean}$) metric during the frost period in this area was larger than in Henan Province and comparable to in Hebei Province, together with lower values of soil moisture and lower amounts of precipitation than in Henan Province. This combination of spatial patterns brought about more intensive frost damage from complex interactions among these factors. On the other hand, although Henan Province maintained the highest values of VI_{bsf}, the accumulated frost degree-days ($AFDD_{mean}$) were the smallest and highest values of soil moisture and precipitation for Henan. Thus, the frost damage to winter wheat was greatly alleviated in the area. For Hebei Province, the accumulated frost degree-days ($AFDD_{mean}$) metric was the largest in comparison those of the other two provinces, but the values of VI_{bsf} were the lowest, indicating the strongest tolerance to frost stress. This interaction limited the frost damage to winter wheat in Hebei Province.

It should be noted that the R^2 in the MLR model was still low ($R^2 = 0.362$). Thus, this model can be used to explore the relationship between various factors and SFDI, but it should not be used as a predictive model because of the overestimation and underestimation of extreme SFDI values (Fig. 7a). First, the relationship between the SFDI and four influential factors was not stable across the study area, and the fitted coefficients of the multiple linear regression model cannot adequately represent the local effects of each factor. Therefore, the fitting accuracy of the MLR model can be greatly improved by implementing the GWR model (Fig. 7b). Second, although ten factors were analyzed, some important factors other than $VI_{bsf\text{-}s}$, SM, $AFDD_{mean}$ and P_t were still not represented. Previous studies have shown that winter wheat varieties, adequate fertilization, cultivation, and seeding quality also play important roles in determining the severity of frost damage (Rozbicki et al., 2015; Sun et al., 2018; Kang et al., 2002). More importantly, cultivar selection is a key factor in determining the low-temperature resistance of winter wheat. Global warming has caused some of the original cultivars to no longer be suitable for continuous planting (Cao et al., 2012; Dai et al., 2014). As a result, the wheat varieties planted in the study area changed from having a strong winter habit to winter or semiwinter habit (e.g., Hebei Province) or even weak spring habit (e.g., Henan Province). These changes in wheat cultivars could lead to different levels of low-temperature resistance and vulnerability to spring frost. Unfortunately, these factors are difficult, if not impossible, to extract from remotely sensed data or field census data over large areas. Introducing these factors in the future is expected to improve the explanatory power of the model. Third, since most of the wheat planting parcels are large in the study area, the effect of mixed pixels can be alleviated to a great extent with the use of coarse-resolution MODIS data, although the influence of mixed pixels cannot be completely avoided. Finer resolution data are more appropriate for areas with heterogeneous wheat planting parcels. Moreover, the spatial mismatch between soil moisture data, MODIS VI data and station meteorological data inevitably increased the uncertainty of the regression analysis.

6. Conclusions

In this study, we proposed a remote sensing-based index (SFDI) that can quantify the continuous impacts of spring frost on winter wheat over a large area rapidly and effectively. Compared with the existing methods, the new index was easy to implement, and the end date can be set flexibly according to the application purpose. It can be used for near real-time or enduring spring frost impact assessments and has the potential to be extended to other agricultural hazards and crop types. The case study using the new index to characterize the spring frost event that occurred from April 3–7, 2018, in North China, showed that the severely damaged areas were mainly located at the junction of Hebei, Henan and Shandong provinces, especially in western Shandong Province. The spatial pattern agreed well with the results of the frost keyword retrieval from newspapers. The effectiveness of SFDI in reflecting the crop yield decline due to the spring frost event was also evaluated with county-level winter wheat yield data. Moreover, we identified that frost damage to winter wheat was not only related to environmental factors, such as accumulated frost degree-days, precipitation, and soil moisture but was also closely related to the growth status of winter wheat (represented by VI_{bsf}) before spring frost occurred. Last, our analysis suggested that reasonable control of excessive crop growth can be a very effective way to alleviate frost damage by limiting the increasing vulnerability of the crop caused by rapid development before the spring frost. Favorable water conditions can also effectively alleviate frost damage; thus, field water management, such as timely irrigation, should be strengthened to reduce frost damage to winter wheat if there is not enough water available during the frost period.

Declaration of Competing Interest

The authors declare that they have no known competing financial interests or personal relationships that could have appeared to influence the work reported in this paper.

Acknowledgements

This study was supported by the National Key Research and Development Program of China (No. 2017YFD0300201).

References

Allevato, E., Saulino, L., Cesarano, G., Chirico, G.B., D'Urso, G., Falanga Bolognesi, S., Rita, A., Rossi, S., Saracino, A., Bonanomi, G., 2019. Canopy damage by spring frost in European beech along the Apennines: effect of latitude, altitude and aspect. Remote Sens. Environ. 225, 431–440. https://doi.org/10.1016/j.rse.2019.03.023.

Barlow, K.M., Christy, B.P., O'Leary, G.J., Riffkin, P.A., Nuttall, J.G., 2015. Simulating the impact of extreme heat and frost events on wheat crop production: A review. F. Crop. Res. 171, 109–119. https://doi.org/10.1016/j.fcr.2014.11.010.

Bascietto, M., Bajocco, S., Ferrara, C., Alivernini, A., Santangelo, E., 2019. Estimating late spring frost-induced growth anomalies in European beech forests in Italy. Int. J. Biometeorol. 63, 1039–1049. https://doi.org/10.1007/s00484-019-01718-w.

Bascietto, M., Bajocco, S., Mazzenga, F., Matteucci, G., 2018. Assessing spring frost effects on beech forests in Central Apennines from remotely-sensed data. Agric. For. Meteorol. 248, 240–250. https://doi.org/10.1016/j.agrformet.2017.10.007.

Bergjord Olsen, A.K., Persson, T., de Wit, A., Nkurunziza, L., Sindhøj, E., Eckersten, H., 2018. Estimating winter survival of winter wheat by simulations of plant frost tolerance. J. Agron. Crop Sci. 204, 62–73. https://doi.org/10.1111/jac.12238.
Brunsdon, C., Fotheringham, A.S., Charlton, M.E., 1996. Geographically Weighted Regression: A Method for Exploring Spatial Nonstationarity. Geogr. Anal. 28, 281–298. https://doi.org/10.1111/j.1538-4632.1996.tb00936.x.
Burke, M.J., Gusta, L.V., Quamme, H.A., Weiser, C.J., Li, P.H., 1976. Freezing and Injury in Plants. Annu. Rev. Plant Physiol. 27, 507–528. https://doi.org/10.1146/annurev.pp. 27.060176.002451.
Cannell, M.G.R., Smith, R.I., 1986. Climatic Warming, Spring Budburst and Forest Damage on Trees. J. Appl. Ecol. 23, 177–191. https://doi.org/10.2307/2403090.
Cao, X., Liu, J., Chen, D., Song, J., Li, H., Liu, A., Zhao, Z., 2012. A Primary Analysis on the Relations between Winter- spring Characteristics Cold Resistance and Wide Adaptation in Winter Wheat. J. Triticeae Crop. 32, 1210–1214. https://doi.org/10.7606/j.issn.1009-1041.2012.06.035.
Charlton, M., Fotheringham, A.S., 2009. Geographically Weighted Regression White Paper. National University of Ireland Maynooth, National Centre for Geocomputation.
Chen, J., Jönsson, P., Tamura, M., Gu, Z., Matsushita, B., Eklundh, L., 2004. A simple method for reconstructing a high-quality NDVI time-series data set based on the Savitzky-Golay filter. Remote Sens. Environ. 91, 332–344. https://doi.org/10.1016/j.rse.2004.03.014.
Chen, J., Rao, Y., Shen, M., Wang, C., Zhou, Y., Ma, L., Tang, Y., Yang, X., 2016. A Simple Method for Detecting Phenological Change From Time Series of Vegetation Index. IEEE Trans. Geosci. Remote Sens. 54, 3436–3449. https://doi.org/10.1109/TGRS.2016.2518167.
Chen, X., Guo, Z., Chen, J., Yang, W., Yao, Y., Zhang, C., Cui, X., Cao, X., 2019. Replacing the Red Band with the Red-SWIR Band (0.74ρred+0.26ρswir) Can Reduce the Sensitivity of Vegetation Indices to Soil Background. Remote Sens. 11, 851. https://doi.org/10.3390/rs11070851.
Crimp, S., Bakar, K.S., Kokic, P., Jin, H., Nicholls, N., Howden, M., 2015. Bayesian space-time model to analyse frost risk for agriculture in Southeast Australia. Int. J. Climatol. 35, 2092–2108. https://doi.org/10.1002/joc.4109.
Crimp, S.J., Zheng, B., Khimashia, N., Gobbett, D.L., Chapman, S., Howden, M., Nicholls, N., 2016. Recent changes in southern Australian frost occurrence: implications for wheat production risk. Crop Pasture Sci. 67, 801–811. https://doi.org/10.1071/CP16056.
Dai, L., Kang, X., Yao, S., Li, C., Yu, C., Wang, M., 2014. Climatic index and risk analysis of winter freezing injury for winter wheat in Hebei. Chinese J. Ecol. 33, 2046–2052. https://doi.org/10.13292/j.1000-4890.2014.0184.
Daoud, J.I., 2017. Multicollinearity and Regression Analysis. J. Phys. Conf. Ser. 949, 012009 https://doi.org/10.1088/1742-6596/949/1/012009.
Dorigo, W., Wagner, W., Albergel, C., Albrecht, F., Balsamo, G., Brocca, L., Chung, D., Ertl, M., Forkel, M., Gruber, A., Haas, E., Hamer, P.D., Hirschi, M., Ikonen, J., de Jeu, R., Kidd, R., Lahoz, W., Liu, Y.Y., Miralles, D., Mistelbauer, T., Nicolai-Shaw, N., Parinussa, R., Pratola, C., Reimer, C., van der Schalie, R., Seneviratne, S.I., Smolander, T., Lecomte, P., 2017. ESA CCI Soil Moisture for improved Earth system understanding: State-of-the art and future directions. Remote Sens. Environ. 203, 185–215. https://doi.org/10.1016/j.rse.2017.07.001.
Dubrule, O., 1984. Comparing splines and kriging. Comput. Geosci. 10, 327–338. https://doi.org/10.1016/0098-3004(84)90030-X.
Duveiller, G., Defourny, P., 2010. A conceptual framework to define the spatial resolution requirements for agricultural monitoring using remote sensing. Remote Sens. Environ. 114, 2637–2650. https://doi.org/10.1016/j.rse.2010.06.001.
Eccel, E., Rea, R., Caffarra, A., Crisci, A., 2009. Risk of spring frost to apple production under future climate scenarios: the role of phenological acclimation. Int. J. Biometeorol. 53, 273–286. https://doi.org/10.1007/s00484-009-0213-8.
Fedoulov, Y.P., 1997. System analysis of frost resistance in winter wheat and its use in breeding. Euphytica. 159–166. https://doi.org/10.1007/978-94-011-4896-2_22.
Fotheringham, A.S., Brunsdon, C., Charlton, M., 2003. Geographically Weighted Regression: The Analysis of Spatially Varying Relationships. John Wiley & Sons. https://doi.org/10.1111/j.1538-4632.2003.tb01114.x.
Frederiks, T.M., Christopher, J.T., Harvey, G.L., Sutherland, M.W., Borrell, A.K., 2012. Current and emerging screening methods to identify post-head-emergence frost adaptation in wheat and barley. J. Exp. Bot. 63, 5405–5416. https://doi.org/10.1093/jxb/ers215.
Frederiks, T.M., Christopher, J.T., Sutherland, M.W., Borrell, A.K., 2015. Post-head-emergence frost in wheat and barley: defining the problem, assessing the damage, and identifying resistance. J. Exp. Bot. 66, 3487–3498. https://doi.org/10.1093/jxb/erv088.
Gao, F., Masek, J., Schwaller, M., Hall, F., 2006. On the blending of the landsat and MODIS surface reflectance: Predicting daily landsat surface reflectance. IEEE Trans. Geosci. Remote Sens. 44, 2207–2218. https://doi.org/10.1109/TGRS.2006.872081.
Gruber, A., Dorigo, W.A., Crow, W., Wagner, W., 2017. Triple Collocation-Based Merging of Satellite Soil Moisture Retrievals. IEEE Trans. Geosci. Remote Sens. 55, 6780–6792. https://doi.org/10.1109/TGRS.2017.2734070.
Gruber, A., Scanlon, T., van der Schalie, R., Wagner, W., Dorigo, W., 2019. Evolution of the ESA CCI Soil Moisture climate data records and their underlying merging methodology. Earth Syst. Sci. Data 11, 717–739. https://doi.org/10.5194/essd-11-717-2019.
Gu, L., Hanson, P.J., Post, W.M., Kaiser, D.P., Yang, B., Nemani, R., Pallardy, S.G., Meyers, T., 2008. The 2007 Eastern US Spring Freeze: Increased Cold Damage in a Warming World? Bioscience 58, 253–262. https://doi.org/10.1641/B580311.
Guy, C.L., 1990. Cold Acclimation and Freezing Stress Tolerance: Role of Protein Metabolism. Annu. Rev. Plant Physiol. Plant Mol. Biol. 41, 187–223. https://doi.org/10.1146/annurev. pp. 41.060190.001155.
Holben, B.N., 1986. Characteristics of maximum-value composite images from temporal AVHRR data. Int. J. Remote Sens. 7, 1417–1434. https://doi.org/10.1080/01431168608948945.
Huang, W., Guan, Q., Luo, J., Zhang, J., Zhao, J., Liang, D., Huang, L., Zhang, D., 2014. New Optimized Spectral Indices for Identifying and Monitoring Winter Wheat Diseases. IEEE J. Sel. Top. Appl. Earth Obs. Remote Sens. 7, 2516–2524. https://doi.org/10.1109/JSTARS.2013.2294961.
Huete, A., Didan, K., Miura, T., Rodriguez, E., Gao, X., Ferreira, L., 2002. Overview of the radiometric and biophysical performance of the MODIS vegetation indices. Remote Sens. Environ. 83, 195–213. https://doi.org/10.1016/S0034-4257(02)00096-2.
Jin, S., 1996. Wheat in China. China Agricultural Press.
Kang, S., Zhang, L., Liang, Y., Hu, X., Cai, H., Gu, B., 2002. Effects of limited irrigation on yield and water use efficiency of winter wheat in the Loess Plateau of China. Agric. Water Manag. 55, 203–216. https://doi.org/10.1016/S0378-3774(01)00180-9.
Klein, R.N., Lyon, D.J., Watkins, J.E., 1994. Freeze injury to Nebraska wheat. Nebraska Cooperative Extension EC, 94–132-S.
Lasdon, L.S., Waren, A.D., Jain, A., Ratner, M., 1978. Design and Testing of a Generalized Reduced Gradient Code for Nonlinear Programming. ACM Trans. Math. Softw. 4, 34–50. https://doi.org/10.1145/355769.355773.
Lazăr, C., Micale, F., Genovese, G., 2005. Simulation of frost resistance of winter wheat in Europe. Ital. J. Agrometeorol. 9, 62–63.
van Leeuwen, W.J., Huete, A.R., Laing, T.W., 1999. MODIS Vegetation Index Compositing Approach. Remote Sens. Environ. 69, 264–280. https://doi.org/10.1016/S0034-4257(99)00022-X.
Li, X., Cai, J., Liu, F., Dai, T., Cao, W., Jiang, D., 2015a. Spring Freeze Effect on Wheat Yield is Modulated by Winter Temperature Fluctuations: Evidence from Meta-Analysis and Simulating Experiment. J. Agron. Crop Sci. 201, 288–300. https://doi.org/10.1111/jac.12115.
Li, Xiangnan, Cai, J., Liu, F., Zhou, Q., Dai, T., Cao, W., Jiang, D., 2015a. Wheat plants exposed to winter warming are more susceptible to low temperature stress in the spring. Plant Growth Regul. 77, 11–19. https://doi.org/10.1007/s10725-015-0029-y.
Li, Xiangnan, Pu, H., Liu, F., Zhou, Q., Cai, J., Dai, T., Cao, W., Jiang, D., 2015b. Winter Wheat Photosynthesis and Grain Yield Responses to Spring Freeze. Agron. J. 107, 1002–1010. https://doi.org/10.2134/agronj14.0460.
Li, Y., Yang, X.G., Dai, S.W., Wang, W.F., 2010. Spatiotemporal evolution characteristics of late spring cold in Guizhou Province under global climate change. Chinese J. Appl. Ecol. 21, 2099–2108. https://doi.org/10.13287/j.1001-9332.2010.0290.
Liu, Q., Piao, S., Janssens, I.A., Fu, Y., Peng, S., Lian, X., Ciais, P., Myneni, R.B., Peñuelas, J., Wang, T., 2018. Extension of the growing season increases vegetation exposure to frost. Nat. Commun. 9, 426. https://doi.org/10.1038/s41467-017-02690-y.
Ma, D., Liu, M., Li, L., Deng, A., 2011. Assessment to impacts of late spring frosts in Hubei province. Chinese J. Agrometeorol. 32, 134–138 https://doi.org/103969/.jissn.1000-6362.2011.01.024.
Mansfield, E.R., Helms, B.P., 1982. Detecting Multicollinearity. Am. Stat. 36, 158. https://doi.org/10.2307/2683167.
Meng, L., Wu, Y., Hu, X., Lv, G., Ren, D., Song, J., 2017. Using Hyperspectral Data for Detecting Late Frost Injury to Winter Wheat under Different Topsoil Moistures. Spectrosc. Spectr. Anal. 37, 1482–1488.
Menzel, A., Helm, R., Zang, C., 2015. Patterns of late spring frost leaf damage and recovery in a European beech (Fagus sylvatica L.) stand in south-eastern Germany based on repeated digital photographs. Front. Plant Sci. 6, 1–14. https://doi.org/10.3389/fpls.2015.00110.
Nolè, A., Rita, A., Ferrara, A.M.S., Borghetti, M., 2018. Effects of a large-scale late spring frost on a beech (Fagus sylvatica L.) dominated Mediterranean mountain forest derived from the spatio-temporal variations of NDVI. Ann. For. Sci. 75, 83. https://doi.org/10.1007/s13595-018-0763-1.
Nuttall, J.G., Perry, E.M., Delahunty, A.J., O'Leary, G.J., Barlow, K.M., Wallace, A.J., 2019. Frost response in wheat and early detection using proximal sensors. J. Agron. Crop Sci. 205, 220–234. https://doi.org/10.1111/jac.12319.
Pettorelli, N., Vik, J.O., Mysterud, A., Gaillard, J.-M., Tucker, C.J., Stenseth, N.C., 2005. Using the satellite-derived NDVI to assess ecological responses to environmental change. Trends Ecol. Evol. 20, 503–510. https://doi.org/10.1016/j.tree.2005.05.011.
Prasad, V.K., Anuradha, E., Badarinath, K.V.S., 2005. Climatic controls of vegetation vigor in four contrasting forest types of India—evaluation from National Oceanic and Atmospheric Administration's Advanced Very High Resolution Radiometer datasets (1990–2000). Int. J. Biometeorol. 50, 6–16. https://doi.org/10.1007/s00484-005-0268-0.
Ql, J., Kerr, Y., 1997. On current compositing algorithms. Remote Sens. Rev. 15, 235–256. https://doi.org/10.1080/02757259709532340.
Rojas, O., Vrieling, A., Rembold, F., 2011. Assessing drought probability for agricultural areas in Africa with coarse resolution remote sensing imagery. Remote Sens. Environ. 115, 343–352. https://doi.org/10.1016/j.rse.2010.09.006.
Rozbicki, J., Ceglińska, A., Gozdowski, D., Jakubczak, M., Cacak-Pietrzak, G., Mądry, W., Golba, J., Piechociński, M., Sobczyński, G., Studnicki, M., Drzazga, T., 2015. Influence of the cultivar, environment and management on the grain yield and bread-making quality in winter wheat. J. Cereal Sci. 61, 126–132. https://doi.org/10.1016/j.jcs.2014.11.001.
Sakamoto, T., 2018. Refined shape model fitting methods for detecting various types of phenological information on major U.S. crops. ISPRS J. Photogramm. Remote Sens. 138, 176–192. https://doi.org/10.1016/j.isprsjprs.2018.02.011.
Sakamoto, T., Gitelson, A.A., Arkebauer, T.J., 2013. MODIS-based corn grain yield estimation model incorporating crop phenology information. Remote Sens. Environ. 131, 215–231. https://doi.org/10.1016/j.rse.2012.12.017.

Sakamoto, T., Wardlow, B.D., Gitelson, A.A., Verma, S.B., Suyker, A.E., Arkebauer, T.J., 2010. A Two-Step Filtering approach for detecting maize and soybean phenology with time-series MODIS data. Remote Sens. Environ. 114, 2146–2159. https://doi.org/10.1016/j.rse.2010.04.019.

Shi, G., 2019. Analysis on Meteorological Conditions of Winter Wheat Growth Period in Shangqiu City in 2017–2018. J. Seed Ind. Guid. 24–28.

de Simões, D.S., Fontana, D.C., Vicari, M.B., 2015. Use of LST images from MODIS/AQUA sensor as an indication of frost occurrence in RS. Rev. Bras. Eng. Agrícola e Ambient. 19, 920–925. https://doi.org/10.1590/1807-1929/agriambi.v19n10p920-925.

Snyder, R.L., Melo-Abreu, J.P. de, 2005. Frost Protection: fundamentals, practice, and economics, Volume 1. Food and Agriculture Organization of the United Nations.

Administration, Standardization, 2017. National standards of the People's Republic of China: Meteorological index of late spring coldness (GB/T 34816–2017). Standards Press of China, Beijing, China.

Sun, S., Yang, X., Lin, X., Sassenrath, G.F., Li, K., 2018. Climate-smart management can further improve winter wheat yield in China. Agric. Syst. 162, 10–18. https://doi.org/10.1016/j.agsy.2018.01.010.

Sutka, J., 1994. Genetic control of frost tolerance in wheat (Triticum aestivum L.). Euphytica 77, 277–282. https://doi.org/10.1007/BF02262642.

Tang, H., Zhou, Q., Liu, J., Li, Z., Wu, W., 2016. Wheat Mapping Using High Resolution Remote Sensing Data. Science Press of China.

Trnka, M., Rötter, R.P., Ruiz-Ramos, M., Kersebaum, K.C., Olesen, J.E., Žalud, Z., Semenov, M.A., 2014. Adverse weather conditions for European wheat production will become more frequent with climate change. Nat. Clim. Chang. 4, 637–643. https://doi.org/10.1038/nclimate2242.

Trought, M., Howell, G.S., Cherry, N., 1999. Practical Considerations for Reducing Frost Damage in Vineyards, New Zealand Winegrowers.

Tucker, C.J., 1979. Red and photographic infrared linear combinations for monitoring vegetation. Remote Sens. Environ. 8, 127–150. https://doi.org/10.1016/0034-4257(79)90013-0.

Wang, C., Chen, J., Wu, J., Tang, Y., Shi, P., Black, T.A., Zhu, K., 2017. A snow-free vegetation index for improved monitoring of vegetation spring green-up date in deciduous ecosystems. Remote Sens. Environ. 196, 1–12. https://doi.org/10.1016/j.rse.2017.04.031.

Wang, H., Wang, J., Wang, Q., Miao, N., Huang, W., Feng, H., Dong, Y., 2012. Hyperspectral characteristics of winter wheat under freezing injury stress and LWC inversion model, in: 2012 First International Conference on Agro- Geoinformatics (Agro-Geoinformatics). IEEE, pp. 1–6. https://doi.org/10.1109/Agro-Geoinformatics.2012.6311627.

Wei, C., Huang, J., Wang, X., Blackburn, G.A., Zhang, Y., Wang, S., Mansaray, L.R., 2017. Hyperspectral characterization of freezing injury and its biochemical impacts in oilseed rape leaves. Remote Sens. Environ. 195, 56–66. https://doi.org/10.1016/j.rse.2017.03.042.

Whaley, J., Kirby, E.J., Spink, J., Foulkes, M., Sparkes, D., 2004. Frost damage to winter wheat in the UK: the effect of plant population density. Eur. J. Agron. 21, 105–115. https://doi.org/10.1016/S1161-0301(03)00090-X.

Xiao, L., Liu, L., Asseng, S., Xia, Y., Tang, L., Liu, B., Cao, W., Zhu, Y., 2018. Estimating spring frost and its impact on yield across winter wheat in China. Agric. For. Meteorol. 260–261, 154–164. https://doi.org/10.1016/j.agrformet.2018.06.006.

Xie, Y., Wang, C., Yang, W., Feng, M., Qiao, X., Song, J., 2020. Canopy hyperspectral characteristics and yield estimation of winter wheat (Triticum aestivum) under low temperature injury. Sci. Rep. 10, 244. https://doi.org/10.1038/s41598-019-57100-8.

Zhang, X., Chen, N., Li, J., Chen, Z., Niyogi, D., 2017. Multi-sensor integrated framework and index for agricultural drought monitoring. Remote Sens. Environ. 188, 141–163. https://doi.org/10.1016/j.rse.2016.10.045.

Zhang, X., Friedl, M.A., Schaaf, C.B., Strahler, A.H., Hodges, J.C.F., Gao, F., Reed, B.C., Huete, A., 2003. Monitoring vegetation phenology using MODIS. Remote Sens. Environ. 84, 471–475. https://doi.org/10.1016/S0034-4257(02)00135-9.

Zhang, X., Yu, W., Wang, C., 2012. Risk Evaluation for Spring Frost Disaster of Winter Wheat in Yellow River-Huai River Regions Based on Crop Model. Plateau Meteorol. 31, 277–284.

Zhao, H., Wang, X., Hu, W., Cao, T., Li, B., 2014. Genetic analysis and countermeasures of wheat late-spring-coldness injury in South Huang-huai Wheat Region. J. Henan Agric. Sci. 43, 34–38. https://doi.org/10.15933/j.cnki.1004-3268.2014.08.010.

Zheng, B., Chapman, S., Christopher, J., Frederiks, T., Chenu, K., 2015. Frost Trends and their Estimated Impact on Yield in the Australian Wheatbelt. Procedia Environ. Sci. 29, 171–172. https://doi.org/10.1016/j.proenv.2015.07.244.

Zheng, D., Yang, X., Mínguez, M.I., Mu, C., He, Q., Wu, X., 2018. Effect of freezing temperature and duration on winter survival and grain yield of winter wheat. Agric. For. Meteorol. 260–261, 1–8. https://doi.org/10.1016/j.agrformet.2018.05.011.

Zhu, X., Helmer, E.H., Gao, F., Liu, D., Chen, J., Lefsky, M.A., 2016a. A flexible spatiotemporal method for fusing satellite images with different resolutions. Remote Sens. Environ. 172, 165–177. https://doi.org/10.1016/j.rse.2015.11.016.